

This is the peer reviewed version of the following article:

Size-dependent commensurability and its possible role in determining the frictional behavior of adsorbed systems / Restuccia, Paolo; Ferrario, Mauro; Sivistrelli, Pier Luigi; Mistura, Giampaolo; Righi, Maria Clelia. - In: PHYSICAL CHEMISTRY CHEMICAL PHYSICS. - ISSN 1463-9076. - 18:41(2016), pp. 28997-29004. [10.1039/C6CP05386F]

*Terms of use:*

The terms and conditions for the reuse of this version of the manuscript are specified in the publishing policy. For all terms of use and more information see the publisher's website.

09/01/2026 10:54

# PCCP

Accepted Manuscript



This article can be cited before page numbers have been issued, to do this please use: P. Restuccia, M. Ferrario, P. L. Silvestrelli, G. Mistura and M. C. Righi, *Phys. Chem. Chem. Phys.*, 2016, DOI: 10.1039/C6CP05386F.



This is an *Accepted Manuscript*, which has been through the Royal Society of Chemistry peer review process and has been accepted for publication.

*Accepted Manuscripts* are published online shortly after acceptance, before technical editing, formatting and proof reading. Using this free service, authors can make their results available to the community, in citable form, before we publish the edited article. We will replace this *Accepted Manuscript* with the edited and formatted *Advance Article* as soon as it is available.

You can find more information about *Accepted Manuscripts* in the [Information for Authors](#).

Please note that technical editing may introduce minor changes to the text and/or graphics, which may alter content. The journal's standard [Terms & Conditions](#) and the [Ethical guidelines](#) still apply. In no event shall the Royal Society of Chemistry be held responsible for any errors or omissions in this *Accepted Manuscript* or any consequences arising from the use of any information it contains.

Cite this: DOI: 10.1039/xxxxxxxxxx

Received Date  
Accepted Date

DOI: 10.1039/xxxxxxxxxx

www.rsc.org/journalname

# Size-dependent commensurability and its possible role in the frictional behavior of adsorbed systems

Paolo Restuccia,<sup>a</sup> Mauro Ferrario,<sup>a</sup> Pier Luigi Sivistrelli<sup>b</sup> Giampaolo Mistura<sup>b</sup> and Maria Clelia Righi<sup>a,c</sup>

Recent nanofriction experiments of xenon on graphene revealed that the slip onset can be induced by increasing the adsorbate coverage above a critical value, which depends on temperature. Moreover, the xenon slippage on gold is much higher than on graphene in spite of the same physical nature of the interactions. To shed light into these intriguing results we have performed molecular dynamics simulations relying on *ab initio* derived potentials. By monitoring the interfacial structure factor as a function of coverage and temperature, we show that the key mechanism to interpret the observed frictional phenomena is the size-dependence of the island commensurability. The latter quantity is deeply affected also by the lattice misfit, which explains the different frictional behavior of Xe on graphene and gold.

## 1 Introduction

Submonolayer islands of rare gas atoms adsorbed on crystal surfaces offer an excellent platform to address friction at crystalline interfaces. In the submonolayer range ( $0 < \theta < 1$ , where  $\theta$  is the coverage) and at low temperatures, adsorbate phase diagrams are well known to display phase-separated two-dimensional (2D) solid islands, usually incommensurate with the surface lattice, coexisting with the 2D adatom vapour.<sup>1</sup> The inertial sliding friction of these islands can be accurately measured with a quartz crystal microbalance (QCM).<sup>2</sup> The condensation of a film on the QCM electrodes is signaled by a decrease in the resonance frequency. Any dissipation taking place at the solid-film interface is instead detected by a decrease in the corresponding resonance amplitude. From the shifts in the resonance frequency and amplitude of the QCM one can calculate the slip time  $\tau_s$ :<sup>3</sup> it represents the time constant of the exponential film velocity decrease due to an hypothetical sudden stop of the oscillating substrate. Very low  $\tau_s$  mean high interfacial viscosity and, in the case of a film rigidly locked to the substrate,  $\tau_s$  goes to zero.

Many different friction phenomena of sub-monolayer islands have been studied with the QCM, including: the dynamic depinning of Kr on gold,<sup>4</sup> the impact of substrate corrugation on the sliding friction levels of adsorbed films,<sup>5</sup> the existence of an onset coverage for sliding of Ne islands on lead,<sup>6</sup> the dynamical

sticking of solid helium on graphite,<sup>7</sup> the nanofriction of various adsorbates on superconducting lead,<sup>8–10</sup> the superlubricity of Xe islands on copper.<sup>11</sup>

The nanotribological studies based on the QCM, which involve clean, well defined interfaces, represent an ideal situation where simulations can combine with experiments to unravel fundamental aspects of friction. Recent findings include the scaling behavior of the island edge contribution to static friction,<sup>12</sup> the effect of non linear dynamics,<sup>13</sup> the influence of the adsorbate-substrate interaction on friction,<sup>14</sup> the size dependence of static friction,<sup>15</sup> the importance of the domain nucleation,<sup>16</sup> the nature of thermally activated island creep<sup>17</sup> and, more in general, the energy dissipation in monolayer films sliding along substrates.<sup>18–20</sup>

Nanoparticle manipulation<sup>21</sup> is also emerging as an invaluable tool to investigate the frictional properties of nanoaggregates on surfaces, both experimentally and by theoretical simulations. Recent findings, complementary and closely related to the QCM ones, include the size-scaling of structural lubricity,<sup>22–24</sup> the influence of contact aging,<sup>25</sup> and thickness promoted lubricity for metallic clusters.<sup>26</sup>

Recently, Pierno *et al.* have measured the sliding time of Xe on graphene with a QCM technique between 25 and 50 K<sup>27</sup> and found that the Xe monolayer is pinned to the graphene surface at temperatures below 30 K. At  $T = 35$  K, the Xe film starts to slide for a coverage of 0.45 monolayer (ML). The critical coverage for sliding decreases with increasing temperature afterwards. By comparison, in similar conditions, the slip times of Xe on the bare gold surface is about twice higher than that on graphene, showing a lower depinning temperature of 25 K. This is counterintuitive since it is believed that the hexagonal graphene layer is

<sup>a</sup>Dipartimento di Scienze Fisiche, Informatiche e Matematiche, Università di Modena e Reggio Emilia, Via Campi 213/A, I-41125 Modena, Italy.

<sup>b</sup>Dipartimento di Fisica e Astronomia, Università di Padova, via Marzolo 8, I-35131, Padova, Italy.

<sup>c</sup>CNR-Institute of Nanoscience, S3 Center, Via Campi 213/A, I-41125 Modena, Italy. E-mail: mariaclelia.righi@unimore.it

smoother for adsorbate than gold surfaces. The understanding of the physical mechanisms behind this puzzling observation is the subject of this theoretical investigation, in which we perform a comparative study of xenon on graphene and on gold substrates. By means of classical molecular dynamics, relying on *ab initio* derived potentials, we simulate the particle diffusion on the two substrates and monitor the commensurability of the growing islands as a function of coverage and temperature.

## 2 Systems & methods

At full monolayer (ML) coverage and temperature below 70 K, the xenon adatoms form a  $(\sqrt{3} \times \sqrt{3})R30^\circ$  sublattice on the graphene layer<sup>28</sup> (GL) (Fig. 1a). The mismatch between the lattice parameters of an isolated Xe monolayer and the graphene  $(\sqrt{3} \times \sqrt{3})R30^\circ$  sublattice is very small, equal to  $-2.8\%$ . The same adsorption configuration for xenon-on-gold (Xe/Au) (Fig. 1b) is characterized by a much larger mismatch, of about  $+13.9\%$ .

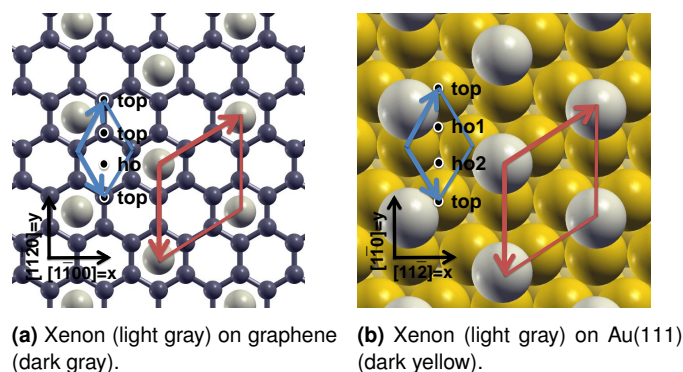


**Fig. 1** (Color online) Xenon atoms arranged in a  $(\sqrt{3} \times \sqrt{3})R30^\circ$  lattice on a graphene layer (a) and Au(111) surface (b). The unit cells of the hexagonal lattices are indicated by arrows, while the labels indicate the location of high symmetry sites.

We sample the potential energy surface (PES), which describes the interaction between the Xe adlayer and the substrate as a function of their relative position, by means of *ab initio* calculations based on density functional theory (DFT). The results are used to optimize the parameters of the interaction potentials subsequently employed in molecular dynamic simulations systems with large number of atoms.

We perform DFT calculations using the Quantum Espresso package,<sup>29</sup> initially within the local density approximation (LDA) for the exchange correlation functional. Afterwards, to better describe the van der Waals (vdW) interactions, the numerical approach has been improved by using the rVV10 density functional.<sup>30</sup> rVV10 denotes a more efficient version of the original VV10 scheme<sup>31</sup> and is based on a nonlocal correlation functional which provides an accurate description of van der Waals effects. rVV10 is expected to perform better than, for instance, PBE-D<sup>32</sup> which is instead a scheme where the semilocal PBE functional is modified by simply adding an empirical potential. This is particularly true for metal and semimetal systems, such as the substrates considered in our study, where the electronic charge density is

relatively delocalized, so that empirical, atom-based vdW corrections turn out to be inadequate.

The ionic species are described by pseudopotentials and the electronic wavefunctions are expanded in plane waves. For the Xe/GL (Xe/Au) system a kinetic energy cutoff of 30 Ry (25 Ry) is used to truncate the expansion on the basis of preliminary calculations optimizing the lattice parameter of graphene (Au). We use periodic supercells with  $(\sqrt{3} \times \sqrt{3})$  in-plane size and vertical edge 42 Å (46 Å) long. The  $\mathbf{k}$ -point sampling of the Brillouin zone is realized with a  $8 \times 8 \times 1$  ( $6 \times 6 \times 1$ ) Monkhorst-Pack grid.<sup>33</sup> The interaction energy per particle,  $E$ , for a Xe layer on the substrate is calculated as  $E = (1/N)[E_{tot} - (E_{sub} + NE_{Xe})]$ , where  $E_{tot}$  is the total energy of the adsorbate system,  $E_{sub}$  is the energy of the isolated substrate and  $E_{Xe}$  is the energy per particle in the isolated xenon layer. All these systems are described with the same  $(\sqrt{3} \times \sqrt{3})$  supercell. The supercell used to model the Xe/GL system contains  $N = 1$  Xe atom, while the supercell used to model the Xe/Au system contains  $N = 2$  Xe atoms adsorbed on the two opposite surfaces of the slab at sites with the same symmetry on the opposite sides. This reduces spurious dipole-dipole interactions between periodically repeated images. The Au slab is 7 layer thick.

Classical molecular dynamics simulations (MD) are performed by using the LAMMPS<sup>34</sup> computer code. The adopted force field are constructed by putting together the following set of interactions. The xenon-xenon interaction is described by the pair potential proposed by Tang and Toennies<sup>35</sup>

$$V_T(\mathbf{r}) = A_T e^{-b_T \mathbf{r}} - \sum_{n=3}^N f_{2n}(b_T \mathbf{r}) \frac{C_{2n}}{\mathbf{r}^{2n}}, \quad (1)$$

where  $\mathbf{r}$  is the distance between two xenon atoms,  $f_{2n}$  is a damping function for the attractive part of the potential that can be expressed in terms of the incomplete gamma function,  $f_{2n}(x) = 1 - \frac{\Gamma(2n+1, x)}{2n!}$ . The adopted numerical values for the  $A_T$ ,  $b_T$  and  $C_{2n}$  coefficients are the same as in the original paper.<sup>35</sup> This potential provides an improved description, with respect to the Lennard Jones potential, of both the repulsive part of the interaction (with the use of the exponential function instead of the too steep  $\mathbf{r}^{-12}$  term) and the attractive part (including the higher order dispersion  $\mathbf{r}^{-8}$  and  $\mathbf{r}^{-10}$  terms in addition to the standard  $\mathbf{r}^{-6}$  one).

The xenon-carbon interaction is described by the functional form of the Buckingham potential<sup>36</sup>

$$V_B(\mathbf{r}) = A_B e^{-b_B \mathbf{r}} - \frac{C_B}{\mathbf{r}^6}; \quad (2)$$

where the  $A_B$ ,  $b_B$  and  $C_B$  coefficients are optimized in order to reproduce the *ab initio* PES, as detailed in Section 3.1. A distance cutoff of 12 Å is used for both the Tang-Toennies and the Buckingham potentials.

The interactions among the carbon atoms of graphene are modelled by the second generation REBO potential.<sup>37,38</sup> To avoid large out-of-plane deformations of the graphene layer and mimic the experimental conditions, we model the presence of a (rigid) substrate underlying the graphene layer by means of the follow-



ing analytic potential:

$$V(x, y, z) = C_0(x, y)e^{-zC_1(x, y)} - \frac{C_2(x, y)}{z^4}, \quad (3)$$

where  $(x, y, z)$  are the coordinates of a carbon atom on the substrate,  $C_i(x, y) = C_i^{\max} - (C_i^{\max} - C_i^{\min})u(x, y)$  for  $i = 0, 1, 2$  with  $u(x, y) = \frac{2}{9}[3 - 2\cos\theta_x\cos\theta_y + \cos 2\theta_y]$ ,  $\theta_x = \frac{2\pi x}{a}$  and  $\theta_y = \frac{2\pi y}{a\sqrt{3}}$ . The numerical values for the  $a$  and  $C_i^{\min/\max}$  coefficients are reported in Ref. 39.

Finally, the interaction of xenon with the Au(111) surface is modeled by the three-dimensional periodic function<sup>40</sup>

$$V(x, y, z) = A_0(x, y)e^{-z(A_1(x, y))} - \frac{A_2(x, y)}{z^3}, \quad (4)$$

where  $A_i(x, y) = A_i^{\text{top}} + \frac{9}{8}(A_i^{\text{ho}} - A_i^{\text{top}})u(x, y)$  for  $i = 1, 2$ , with  $u(x, y) = [3 - \sum_{\mathbf{g}} \cos \mathbf{g} \cdot \mathbf{r}]$  and the summation running over the first three  $\mathbf{g}$  vector of the reciprocal lattice and  $A_0(x, y)$  is given by

$$A_0(x, y) = A_0^{\text{top}} \exp \left[ \frac{A_1(x, y) - A_1^{\text{top}}}{A_1^{\text{ho}} - A_1^{\text{top}}} \ln \left( \frac{A_0^{\text{ho}}}{A_0^{\text{top}}} \right) \right]. \quad (5)$$

This function is able to accurately describe the peculiar features of the PES for rare gases on metals.<sup>40,41</sup> In particular, its “anticorrugation”, which originates from the on-top site preference for rare gas adsorption rather than hollow site.<sup>42,43</sup> This feature can not be reproduced by pair-wise potentials, such as the Lennard-Jones potential, that favor adsorption at the highest coordinated sites. The numerical parameters entering the  $A_i(x, y)$  periodic functions are determined by fitting *ab initio* adsorption energies calculated for several configurations of the xenon atom on the metal surface, as described in the next section.

MD calculations are performed using periodic boundary conditions. The orthorhombic cell used to model the Xe/GL (Xe/Au) system has 15.25 nm × 14.67 nm × 2.00 nm (18.17 nm × 17.48 nm × 2.00 nm) dimensions. We consider three different Xe coverages both on the GL and Au(111) surface. The adatom coverage is calculated assuming that  $\theta = 100\%$  corresponds to a complete Xe ML with an areal density of 5.94 atoms/nm<sup>2</sup>, i. e., considering a nearest neighbor distance among Xe atoms of 0.44 nm. This choice is consistent with that adopted in the analysis of the QCM experiments.<sup>27</sup> The simulated coverages  $\theta = 11\%, 22\%, 44\%$  correspond, thus, to 147, 294, 588 adparticles in the Xe/GL system, and to 208, 416, 832 particles in the Xe/Au system, being 1328 and 1886 the total numbers of atoms necessary to realize a 100% coverage of the two-dimensional cells used in the two systems.

The MD simulations are started from initial conditions constructed by assigning to the xenon atoms random, non-overlapping, positions on the surface, and random velocities sampled from the Maxwell distribution at the temperature  $T_o = 25$  K. The system is then thermalized at  $T_\ell = 30$  K with a constant-volume, constant-temperature (NVT) run, 10 ns long. A second, higher temperature value,  $T_h = 50$  K, is also considered to match the experimental conditions, where both  $T_\ell$  and  $T_h$  are considered. The initial configurations at  $T_h$  are generated from those at

the end of the  $T_\ell$  runs, by increasing sharply the temperature and letting the systems equilibrate for further 10 ns. The temperature is controlled by means of Langevin thermostats,<sup>44</sup> with two separate thermostats used for the Xe/GL system, one for each atomic species, and only one for the Xe/Au system. The same integration time step  $\delta t = 1$  fs is used in all calculations.

## 3 Results & discussion

### 3.1 Sampling the PES for xenon on graphene and gold by *ab initio* calculations

We calculate the Xe adsorption energy on graphene and gold substrates for different relative positions, obtaining in this way a sampling of the PESes for the two adsorbate systems shown in Fig. 1. We firstly perform standard DFT calculations with the exchange correlation functional described by LDA. Then, we take into account the vdW interactions by means of the rVV10 method,<sup>30</sup> as motivated in the previous section. The results obtained within rVV10 are used as benchmark to derive the parameter values for the xenon-carbon (Eq. 2) and xenon-Au(111) (Eq. 4) potentials used in the MD simulations.

The calculated interaction energy,  $E$ , between the Xe adatom and the substrate (see Section 2 for the definition of  $E$ ) is represented as a function of the adatom-substrate separation,  $z$ , in Fig. 2a and 2b. The Xe atom position relative to the substrate corresponds to the most favorable one in both the cases. By comparing the red and green curves, it appears evident that the DFT-LDA description underestimates the depth of the potential wells, a problem which is solved by the rVV10 method that increases the strength and widens the range of the attractive part of the interactions. The equilibrium distance,  $z_{eq}$ , and the corresponding energy in the minimum, i.e., the adsorption energy  $E_{ads}$ , are reported in Table 1 both for the Xe/GL and Xe/Au systems. It can be seen that absolute value of the adsorption energy of Xe on gold substrate is significantly higher, about 100 meV per atom, compared with that on graphene substrate; this is most likely due to the partial hybridization of Xe 5p orbitals with Au d states.<sup>45,46</sup> The equilibrium adsorption energies and distances are in good agreement with previous experimental and theoretical data. In particular, the Xe adsorption energy on graphene,  $E_{ads}^{GL} = -197$  meV/atom, is within the range of theoretical data available in the literature ( $-128.6$  meV/atom by DFT/vdW-WF<sup>47</sup>,  $-142.9$  meV/atom by MP2,<sup>48</sup>  $-204$  meV/atom by all-electron full-potential linearized augmented plane wave plus local orbitals method<sup>49</sup> and  $-209.7$  meV/atom by DFT/vdW-DF method<sup>46</sup>), and the adsorption distance,  $z_{eq}^{GL} = 3.61$  Å, is in excellent agreement with the experimental value of  $3.59 \pm 0.04$  Å. In the case of the Xe/Au system, our adsorption energy,  $E_{ads}^{GL} = -289$  meV/atom, is in good agreement with previous theoretical calculations ( $-262.3$  meV/atom by DFT/vdW-DF<sup>46</sup>) and within the experimental range,<sup>50–53</sup> while the equilibrium distance,  $z_{eq}^{Au} = 3.43$  Å, is slightly shorter than the experimental ( $3.62$  Å) and theoretical ( $3.58$  Å) values reported in the literature.<sup>46,50</sup>

We then calculate the Xe-substrate interaction energy for different relative lateral positions. In particular, we consider the configurations along the direction (referred to as  $y$  direction)

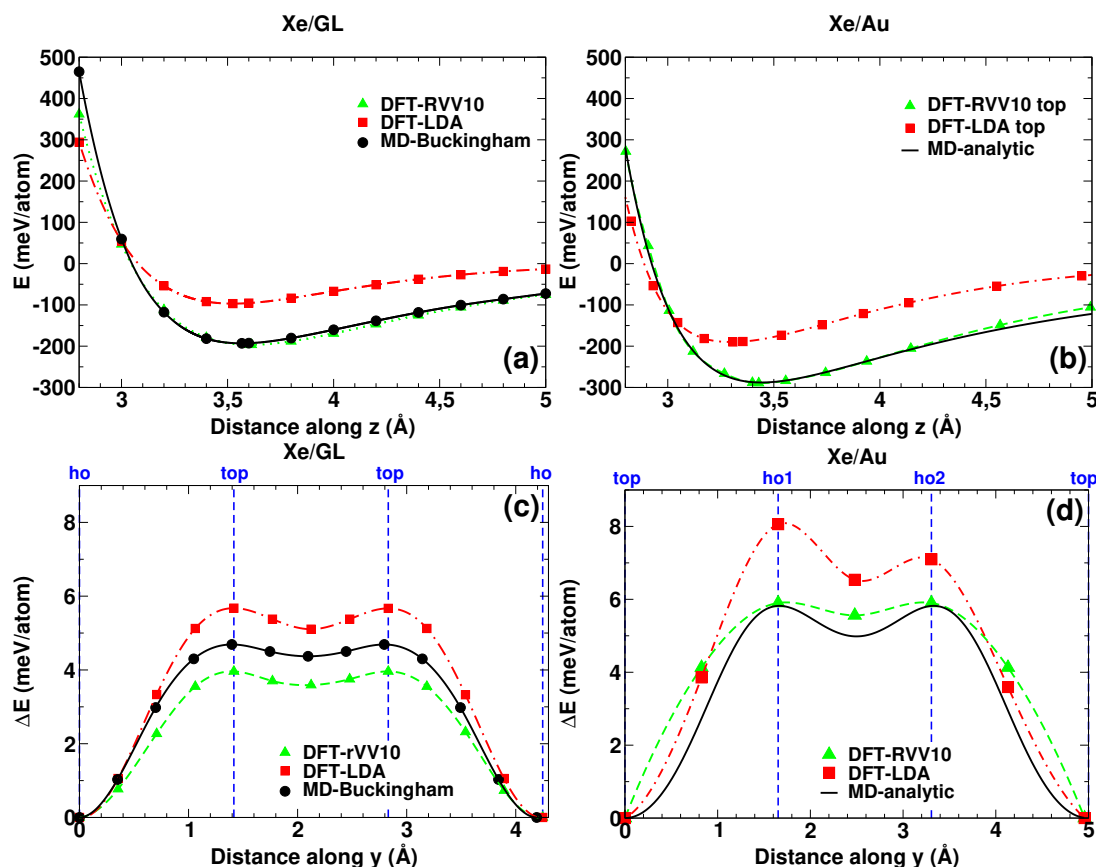


**Fig. 2** (Color online) Interaction energy between Xe and graphene (gold) as a function of the separation (a, b) and the relative lateral position (c, d). The latter spans the high symmetry sites labelled according to Fig. 1.

passing through the high symmetry sites labelled in Fig. 1. The Xe-substrate distance is optimized at each location. The energy profile obtained for the Xe/GL system, represented in Fig. 2c, presents the minima (maxima) at hollow (on-top) sites. On the contrary, the energy profile obtained for the Xe/Au system presents the minima (maxima) at on-top (hollow) sites, in agreement with experimental observations. The energy difference between the maxima and the minima ( $\Delta E$ ), referred to as the PES corrugation, is reported in Table 1. The PES corrugation calculated within both the DFT schemes is slightly higher for the Xe/Au system than Xe/GL. The order of magnitude of the PES corrugations is the same as those estimated from experiments. This is consistent with the fact that Xe presents a stronger binding on gold than on graphene. It is, in fact, often observed that the energy barriers to displace an adsorbate (or a countersurface) along a substrate increase with the strength of the adsorbate-substrate interaction.

The results obtained within the DFT-rVV10 scheme for the adsorption of Xe on both graphene and gold substrates appear to be accurate enough to be used as the reference dataset for tuning the unknown parameters appearing in the force field for the Xe-C (Eq. (2)) and Xe-Au (Eq. (4)) interactions. By fitting the data shown in Fig. 2a and 2b with a nonlinear least-squares Marquardt-Levenberg algorithm,<sup>56</sup> we obtain the parameter values reported in Table 2. The fitting is very satisfactory as can be

seen in Fig. 2a and 2b by comparing the Xe adsorption energy as a function of the adatom-substrate separation calculated within the MD scheme (in black color) with the *ab initio* rVV10 data (in green color); in particular the equilibrium energies and distances are in excellent agreement. The energy variation as a function of the adatom lateral position, shown in Fig. 2c and 2d, is well reproduced by the adopted force fields. An accurate description of the lateral PES is essential for a reliable simulation of tribological systems. The shape and the corrugation of the PES determine, in fact, the frictional forces. It is typically difficult to correctly reproduce the shape of the PES for rare gases on metals by analytical force fields. Pair wise potentials, like the Lennard Jones potential, favor, in fact, the sites with the highest coordination. Experiments reveal, instead, that for many rare gas atoms on metals, such as Xe on gold, the adsorption occurs on-top. Such hard substrates can be accurately modeled by an external potential representing the interaction with a fixed and rigid triangular lattice frame.<sup>12,40</sup> The potential we adopted to model the Xe/Au system correctly reproduce the PES shape (Fig. 2c), with minima at on-top sites and maxima at hollow sites. Not only, the potential corrugation is in excellent agreement with that obtained by the rVV10 method. A small underestimation, less than 1 meV, is instead observed in the PES corrugation for the Xe/GL system. The uncertainty in the estimation of the PES corrugation is not expected to affect the results of the MD simulations presented in the next section. The

**Table 1** Optimized adsorption distance,  $z_{eq}$  (Å), adsorption energy,  $E_{ads}$  (meV/atom), and potential corrugation,  $\Delta E$  (meV), for xenon on graphene and gold. The DFT results obtained within the LDA and rVV10 approaches are compared to other theoretical and experimental data present in the literature.

	$z_{eq}^{GL}$	$z_{eq}^{Au}$	$E_{ads}^{GL}$	$E_{ads}^{Au}$	$\Delta E^{GL}$	$\Delta E^{Au}$
DFT-LDA	3.53	3.31	−97	−190	6	8
DFT-rVV10	3.61	3.43	−197	−289	4	6
Theory	$3.56 \pm 4.18^{a,b,c}$	$3.58^a$	$-128.6 \div -209.7^{a,b,c,d}$	$-262.3^a$	$3.1 \div 15.5^{a,c,e}$	$2.7^a$
Experiments	$3.59 \pm 0.04^f$	$3.62^g$	—	$-199.5 \div -363^{g,h,i,j}$	$3.29 \div 5.3^{k,l,m}$	$2.2^l$

<sup>a</sup>Ref. 46, <sup>b</sup>Ref. 47, <sup>c</sup>Ref. 48, <sup>d</sup>Ref. 49, <sup>e</sup>Ref. 54, <sup>f</sup>Ref. 28 for Xe/graphite, <sup>g</sup>Ref. 50, <sup>h</sup>Ref. 51, <sup>i</sup>Ref. 52, <sup>j</sup>Ref. 53, <sup>k</sup>Ref. 5, <sup>l</sup>Ref. 27, <sup>m</sup>Ref. 55 for Xe/graphite

**Table 2** Values of the  $A_B, b_B, C_B$  parameters for the Xe-C interaction and of the  $A_0, A_1, A_2$  coefficients in the functions  $A_i(x, y)$  for the Xe-Au(111) interaction.

Xe-C			
Buckingham	$A_B$ (eV)	$b_B(\text{\AA}^{-1})$	$C_B(\text{eV} \cdot \text{\AA}^6)$
	$1.835 \cdot 10^4$	0.273	76.494
Xe-Au(111)			
Analytic	$A_0$ (eV)	$A_1$ (Å)	$A_2$ (eV · Å <sup>3</sup> )
<i>top</i>	$3.88 \cdot 10^4$	3.78	15.24
<i>ho</i>	$3.13 \cdot 10^3$	2.99	15.79

different lattice match of the Xe/Au and Xe/GL plays, in fact, the major role in determining the degree of commensurability of the rare gas islands in the two systems.

In conclusion, the parametric potentials tuned on the DFT-rVV10 data provide an accurate description of the adsorbate systems. Their use in MD simulations will allow us to study the evolution of a system relevant for tribology, containing a large number of xenon atoms over long time scales, typically inaccessible by *ab initio* MD.<sup>57,58</sup>

### 3.2 Monitoring the commensurability of the adsorbed monolayers by molecular dynamics

Classical molecular dynamics simulation runs, each 20 ns long, for three coverage values and two different temperatures have been analyzed in parallel for the Xe/GL and Xe/Au systems. The final atomic configurations of all the simulated systems are pictured in Fig. 3 using a range of gray shades from black to white to illustrate the different level of commensurability between the xenon layer and the substrates below: black color means that the adatom is commensurate with respect to the substrate (i.e. resides in a minimum of the potential); white color means that the adatom is fully incommensurate (i.e. is located in a maximum of the potential), gray levels represent intermediate conditions.

In both the studied systems, it is possible to notice that the xenon atoms at low temperature and low coverage gather into many separated islands of small size with the characteristic hexagonal pattern. In the Xe/GL case there is a predominance of black as the Xe atoms tend to register with the minima of the PES; in this case the mismatch of the lattices is small and the

number of neighbors of each Xe atoms is not enough to provide the energy gain to promote incommensurability between the Xe and GL lattices. For Xe/Au system, instead, while the size of the island is comparable, the presence of black Xe atoms is much less relevant.

With increasing temperature, one can see immediately that the size of these islands increases in all cases, as the increase of thermal energy makes easier for the Xe atoms to overcome the energy barriers of the PES and Xe diffusion on the surface is correspondingly enhanced. The grayscale patterns do not change significantly for the Xe/Au systems, but for the Xe/GL systems one can immediately notice a lower presence of neighboring black Xe atoms.

As expected, increasing the coverage leads to an increase of the size of the clusters. In particular, while at 11% and 22% coverage one can count several isolated ones, at 44% for both systems Xe atoms are arranged in a unique connected cluster, i.e., the size of the island reaches the dimension of the MD cell. In the Xe/Au case there are mainly isolated black Xe atoms in register with the PES minima while for Xe/GL several, somewhat smaller, black patches remain.

Overall one sees that the size of these xenon cluster increases both with coverage and temperature and, correspondingly, their structure becomes more and more incommensurate with the substrate. The change in the range of temperature and coverage explored is more significant for the Xe/GL system, where the mismatch between the Xe and the substrate is smaller, favoring the existence of small commensurate islands at lower temperatures and coverages. This qualitative behavior of the adatoms can be confirmed quantitatively by computing the structure factor  $S(\mathbf{G})$  of the xenon atoms

$$S(\mathbf{G}) = \sqrt{\frac{|\sum_{j=1}^N e^{i\mathbf{G} \cdot \mathbf{r}_j}|^2}{N^2}} \quad (6)$$

where  $\mathbf{G}$  is the summation of the two reciprocal lattice basis vectors of the substrate cell and  $\mathbf{r}_j$  is the real space position of the  $j$ -th xenon atom.  $S(\mathbf{G})$  crosses over from  $\sim 0$ , for fully incommensurability, to 1 for fully commensurability. In panel (a) of Fig. 4 we report the behaviors of each individual  $S(\mathbf{G})$  as a function of time, together with the averaged values of  $S(\mathbf{G})$  over the last 10 ns of the simulations for both systems. It is possible to notice that, by varying the coverage and the temperature of the systems,  $S(\mathbf{G})$  changes significantly; in particular, at low coverage and low tem-



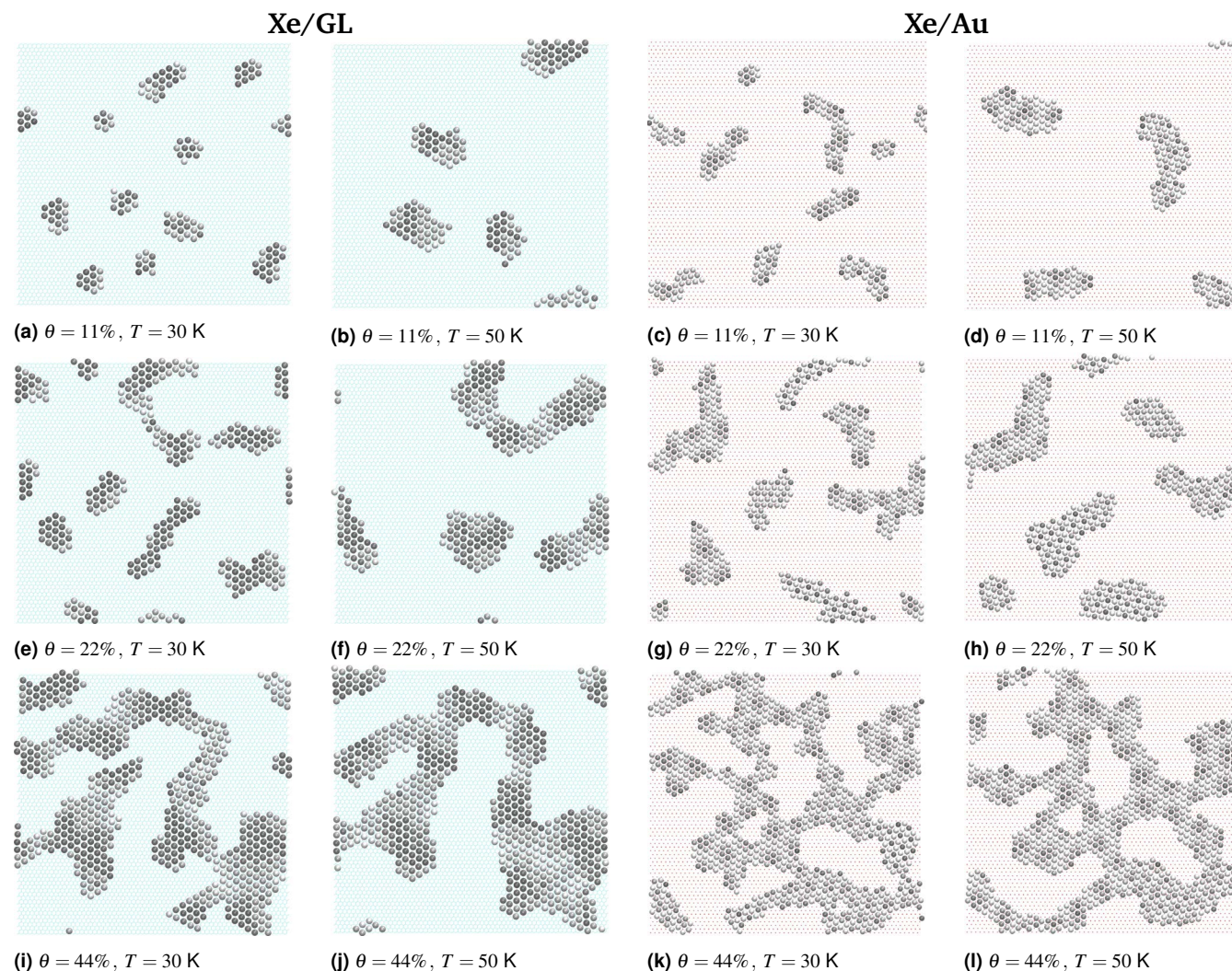


**Fig. 3** (Color online) Snapshots of the simulation cell for the Xe/GL and Xe/Au systems at the end of MD simulations each lasted 20 ns. The simulated coverage,  $\theta$ , and temperature,  $T$ , are indicated in each figure panel. The Xe particles are colored according to their position on the PES: a grayscale is used to indicate the particle distance from the PES minima (maxima), in black (white).

perature,  $S(\mathbf{G})$  attains its maximum, instead at high coverage and temperature,  $S(\mathbf{G})$  decreases significantly in both systems. Moreover,  $S(\mathbf{G})$  is always higher in the Xe/GL system than in Xe/Au one. These data allow us to confirm quantitatively the qualitative analysis based on the final atomic configurations.

Our results complemented with a previous study, where we described the close relation between the commensurability and static friction of adsorbed islands,<sup>15</sup> can provide an explanation for the QCM experimental observations reported in Ref. 27. In particular, (i) the existence of pinning forces in nominally incommensurate systems at low coverage can be accounted for by the result that small adsorbed islands are commensurate with the substrate even in the presence of lattice misfit. (ii) The existence of a critical coverage necessary for the film slipping is related to the critical size that the growing Xe islands need to reach for the depinning process to be activated at the considered temperature. (iii) Lower critical coverages are observed for Xe/Au than Xe/GL in spite of the larger PES corrugation of the former

system because the lattice misfit has a larger impact on the commensurability of islands. We showed, in fact, that the critical size for adsorbed island,  $R_C \sim \frac{1}{\epsilon^2} \sqrt{\frac{\Delta E}{\epsilon}}$ , depends on the ratio between the potential corrugation,  $\Delta E$ , and the interparticle interaction strength  $\epsilon$ , and is dominated by the lattice misfit,  $e$ .<sup>15</sup> We expect that the above result can be generalized to solid clusters on crystalline substrates: clusters will interlock with substrates if their size shrinks to a critical value. How small is this value depends on the bulk modulus, interfacial corrugation and lattice mismatch. An example of this situation may be provided by AFM tips that quite often display a stick-and-slip behavior, due to interlocking, independently from the nominal incommensurability of the tip and the substrate materials.

## 4 Conclusions

In a recent experiment,<sup>27</sup> the nanofriction of Xe monolayers deposited on graphene has been measured by means of quartz crystal microbalance. At low temperatures, the adsorbate was fully

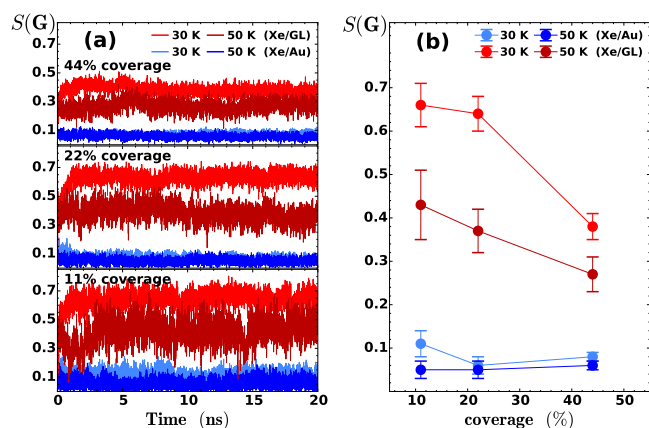


**Fig. 4** (Color online) The average structure factor  $S(G)$  for the Xe/GL and Xe/Au systems (a) as a function of the time and (b) evaluated averaging over the last 10 ns of the simulation. The two different scales of red (blue) represent the two different temperatures used during the simulations for the Xe/GL (Xe/Au) system. Reported error bars correspond to the standard deviations.

pinned to the substrate, it started sliding as soon as a critical coverage was reached. The critical coverage was found to depend on the temperature, in particular it decreases with the temperature. Similar measurements repeated on bare gold showed an enhanced slippage of the Xe films and a decrease of the depinning temperature.

To shed light into the atomistic mechanism governing the above described experimental observations, we have performed a comparative study of xenon dynamics on graphene and gold substrates at different coverages and temperatures. The first part of our work is devoted to the accurate theoretical description of the Xe-graphene and Xe-Au(111) interactions. Our DFT calculations show that the rVV10 method,<sup>30</sup> which allows to treat non-local van der Waals interactions from first principles, improves the LDA description and provides adsorption energies and distances in very good agreement with the available experimental data. The DFT rVV10 results are used to optimize the force fields employed in the MD simulations. An excellent fit of the PES for the Xe/GL system is obtained by using the Buckingham pairwise potential for the Xe-C interactions, while the Xe-Au(111) interaction is accurately described by means of the analytic function proposed in Ref. 40 for rare gas on metals.

The MD simulations performed in the second part of our work show that at low temperatures and coverages the Xe atoms deposited on graphene cluster in small islands. The island size increases with the temperature due to an increased particle diffusion on the substrate. The island size increases also with coverage until the Xe layer percolates and a unique patch of coalesced islands is formed. We monitor the island commensurability during their growth both by a visual and quantitative method based on the calculated structure factor. The results uncover the existence of a close correlation between the island size and commensurability: small islands are in registry with the substrate, while larger islands are less commensurate. The simulations repeated in equivalent conditions on gold reveal a similar trend, but a much lower

commensurability is found for every considered temperature and coverage.

Considering the close relation between the static friction and the interfacial commensurability,<sup>15</sup> our results can explain the existence of a critical coverage for the depinning transition and its dependence on temperature as observed in QCM experiments.<sup>27</sup> Furthermore, they confirm the theory on the size dependence of static friction, according to which nominal incommensurate interfaces becomes commensurate below a critical size.<sup>15</sup> The critical size, that depends on the interparticle interaction strength and the potential corrugation, is dominated by the lattice misfit. The latter dependence accounts for the different frictional behavior observed for the Xe/GL and Xe/Au systems.

## 5 Acknowledgments

We acknowledge the CINECA consortium for the availability of high performance computing resources and support through the ISCRA-A “Lubric” project.

## References

- 1 L. W. Bruch, R. D. Diehl and J. A. Venables, *Rev. Mod. Phys.*, 2007, **79**, 1381–1454.
- 2 J. Krim and A. Widom, *Phys. Rev. B*, 1988, **38**, 12184–12189.
- 3 L. Bruschi and G. Mistura, *Phys. Rev. B*, 2001, **63**, 235411.
- 4 L. Bruschi, A. Carlin and G. Mistura, *Phys. Rev. Lett.*, 2002, **88**, 046105.
- 5 T. Coffey and J. Krim, *Phys. Rev. Lett.*, 2005, **95**, 076101.
- 6 L. Bruschi, G. Fois, A. Pontarollo, G. Mistura, B. Torre, F. Buatier de Mongeot, C. Boragno, R. Buzio and U. Valbusa, *Phys. Rev. Lett.*, 2006, **96**, 216101.
- 7 N. Hosomi, J. Taniguchi, M. Suzuki and T. Minoguchi, *Phys. Rev. B*, 2009, **79**, 172503.
- 8 A. Dayo, W. Alnasrallah and J. Krim, *Phys. Rev. Lett.*, 1998, **80**, 1690–1693.
- 9 R. L. Renner, P. Taborek and J. E. Rutledge, *Phys. Rev. B*, 2001, **63**, 233405.
- 10 M. Pierno, L. Bruschi, G. Fois, G. Mistura, C. Boragno, F. B. de Mongeot and U. Valbusa, *Phys. Rev. Lett.*, 2010, **105**, 016102.
- 11 M. Pierno, L. Bruschi, G. Mistura, G. Paolicelli, A. di Bona, S. Valeri, R. Guerra, A. Vanossi and E. Tosatti, *Nat. Nanotechnol.*, 2015, **10**, 714–718.
- 12 N. Varini, A. Vanossi, R. Guerra, D. Mandelli, R. Capozza and E. Tosatti, *Nanoscale*, 2015, **7**, 2093–2101.
- 13 N. Manini, O. M. Braun, E. Tosatti, R. Guerra and A. Vanossi, *Journal of Physics: Condensed Matter*, 2016, **28**, 293001.
- 14 Y. N. Zhang, F. Hanke, V. Bortolani, M. Persson and R. Q. Wu, *Phys. Rev. Lett.*, 2011, **106**, 236103.
- 15 M. Reguzzoni and M. C. Righi, *Phys. Rev. B*, 2012, **85**, 201412.
- 16 M. Reguzzoni, M. Ferrario, S. Zapperi and M. C. Righi, *Proceedings of the National Academy of Sciences*, 2010, **107**, 1311–1316.
- 17 B. Persson, O. Albohr, F. Mancosu, V. Peveri, V. Samoilov and I. Sivebaek, *Wear*, 2003, **254**, 835–851.



- 18 E. D. Smith, M. O. Robbins and M. Cieplak, *Phys. Rev. B*, 1996, **54**, 8252–8260.
- 19 A. Vanossi, N. Manini, M. Urbakh, S. Zapperi and E. Tosatti, *Rev. Mod. Phys.*, 2013, **85**, 529–552.
- 20 J. Krim, *Advances in Physics*, 2012, **61**, 155–323.
- 21 D. Dietzel, T. M  nninghoff, L. Jansen, H. Fuchs, C. Ritter, U. D. Schwarz and A. Schirmeisen, *Journal of Applied Physics*, 2007, **102**, 084306.
- 22 A. S. de Wijn, *Phys. Rev. B*, 2012, **86**, 085429.
- 23 D. Dietzel, M. Feldmann, U. D. Schwarz, H. Fuchs and A. Schirmeisen, *Phys. Rev. Lett.*, 2013, **111**, 235502.
- 24 D. Dietzel, U. D. Schwarz and A. Schirmeisen, *Friction*, 2014, **2**, 114–139.
- 25 T. A. Sharp, L. Pastewka and M. O. Robbins, *Phys. Rev. B*, 2016, **93**, 121402.
- 26 R. Guerra, E. Tosatti and A. Vanossi, *Nanoscale*, 2016, **8**, 11108–11113.
- 27 M. Pierno, L. Bignardi, M. C. Righi, L. Bruschi, S. Gottardi, M. Stohr, O. Ivashenko, P. L. Silvestrelli, P. Rudolf and G. Mistura, *Nanoscale*, 2014, **6**, 8062–8067.
- 28 K. Pussi, J. Smerdon, N. Ferralis, M. Lindroos, R. McGrath and R. Diehl, *Surface Science*, 2004, **548**, 157 – 162.
- 29 P. Giannozzi *et al.*, *Journal of Physics: Condensed Matter*, 2009, **21**, 395502.
- 30 R. Sabatini, T. Gorni and S. de Gironcoli, *Phys. Rev. B*, 2013, **87**, 041108.
- 31 O. A. Vydrov and T. Van Voorhis, *The Journal of Chemical Physics*, 2010, **133**, 244103.
- 32 S. Grimme, *Journal of Computational Chemistry*, 2006, **27**, 1787–1799.
- 33 H. J. Monkhorst and J. D. Pack, *Phys. Rev. B*, 1976, **13**, 5188–5192.
- 34 S. Plimpton, *Journal of Computational Physics*, 1995, **117**, 1 – 19.
- 35 K. T. Tang and J. P. Toennies, *The Journal of Chemical Physics*, 2003, **118**, 4976–4983.
- 36 R. A. Buckingham, *Proceedings of the Royal Society of London A: Mathematical, Physical and Engineering Sciences*, 1938, **168**, 264–283.
- 37 D. W. Brenner, O. A. Shenderova, J. A. Harrison, S. J. Stuart, B. Ni and S. B. Sinnott, *Journal of Physics: Condensed Matter*, 2002, **14**, 783.
- 38 S. J. Stuart, A. B. Tutein and J. A. Harrison, *The Journal of Chemical Physics*, 2000, **112**, 6472–6486.
- 39 M. Reguzzoni, A. Fasolino, E. Molinari and M. C. Righi, *Phys. Rev. B*, 2012, **86**, 245434.
- 40 M. C. Righi and M. Ferrario, *J. Phys.: Condens. Matter*, 2007, **19**, 305008.
- 41 M. C. Righi and M. Ferrario, *Phys. Rev. Lett.*, 2007, **99**, 176101.
- 42 J. L. F. Da Silva and C. Stampfl, *Phys. Rev. B*, 2007, **76**, 085301.
- 43 J. L. F. D. Silva, C. Stampfl and M. Scheffler, *Phys. Rev. Lett.*, 2003, **90**, 066104.
- 44 T. Schneider and E. Stoll, *Phys. Rev. B*, 1978, **17**, 1302–1322.
- 45 Y. N. Zhang, V. Bortolani and G. Mistura, *Phys. Rev. B*, 2014, **89**, 165414.
- 46 Y. N. Zhang, V. Bortolani and G. Mistura, *Journal of Physics: Condensed Matter*, 2014, **26**, 445003.
- 47 A. Ambrosetti and P. L. Silvestrelli, *The Journal of Physical Chemistry C*, 2011, **115**, 3695–3702.
- 48 L. Sheng, Y. Ono and T. Taketsugu, *The Journal of Physical Chemistry C*, 2010, **114**, 3544–3548.
- 49 J. L. F. Da Silva and C. Stampfl, *Phys. Rev. B*, 2007, **76**, 085301.
- 50 B. Nieuwenhuys, O. V. Aardenne and W. Sachtler, *Chemical Physics*, 1974, **5**, 418 – 428.
- 51 C. H  ckst  dt, S. Schmidt, S. H  fner, F. Forster, F. Reinert and M. Springborg, *Phys. Rev. B*, 2006, **73**, 075409.
- 52 F. Forster, A. Bendounan, J. Ziroff and F. Reinert, *Surface Science*, 2006, **600**, 3870 – 3874.
- 53 T. Andreev, I. Barke and H. H  vel, *Phys. Rev. B*, 2004, **70**, 205426.
- 54 W. A. Steele, *Surface Science*, 1973, **36**, 317 – 352.
- 55 H. Hong, C. J. Peters, A. Mak, R. J. Birgeneau, P. M. Horn and H. Suematsu, *Phys. Rev. B*, 1989, **40**, 4797–4807.
- 56 W. H. Press, S. A. Teukolsky, W. T. Vetterling and B. P. Flannery, *Numerical Recipes. The Art of Scientific Computing*, 3rd edition, Cambridge University Press, Cambridge, 2007.
- 57 R. Car and M. Parrinello, *Phys. Rev. Lett.*, 1985, **55**, 2471–2474.
- 58 G. Zilibotti, S. Corni and M. C. Righi, *Phys. Rev. Lett.*, 2013, **111**, 146101.